Abruptly autofocusing property and optical manipulation of circular Airy beams

Wanli Lu,[1] Xu Sun,[1] Huajin Chen,[2,3,*] Shiyang Liu,[4,†] and Zhifang Lin[3,5,6]

[1]*School of Physical Science and Technology, China University of Mining and Technology, Xuzhou, Jiangsu 221116, China*
[2]*School of Electrical and Information Engineering, Guangxi University of Science and Technology, Liuzhou, Guangxi 545006, China*
[3]*State Key Laboratory of Surface Physics and Department of Physics, Fudan University, Shanghai 200433, China*
[4]*Institute of Information Optics, Zhejiang Normal University, Jinhua, Zhejiang 321004, China*
[5]*Key Laboratory of Micro and Nano Photonic Structures, Fudan University, Shanghai 200433, China*
[6]*Collaborative Innovation Center of Advanced Microstructures, Nanjing University, Nanjing 210093, China*

(Received 29 August 2018; published 10 January 2019)

By employing the angular spectrum representation, we successfully derive the partial-wave expansion coefficients of the circular Airy beams (CABs) with different polarizations, based on which the scattering of a spherical particle in the CABs is solved exactly. Special attention is focused on exploring the potential applications of the CABs in the abruptly autofocusing (AAF) property and optical manipulation of microparticle by optical force. It is found that both the linear and circular polarizations are the best candidates to implement the AAF property robustly against strong disturbance by a large-sized particle. In addition, although the CABs can be intensively focused to a small region, resulting in an abrupt increase of light intensity by two orders of magnitude at the focal point and enabling three-dimensional stable trapping of a Rayleigh particle near the focal point, the usual CABs fail to generate an optical force outweighing the Brownian force to achieve a stable transverse trapping in the region before the focal point. On the other hand, a Mie particle can be confined transversely in the primary ring and accelerated along the curved trajectory of CABs to the focal point, then pushed further all the way through the focal point rather than being trapped therein, and eventually accelerated further along a straight trajectory in the direction of light propagation over 100 wavelengths, due to the weak diffraction characteristic of a morphed Bessel-like beam of CABs. The exotic curved-straight trajectory transport of particles by the CABs may find applications in the case where the transport path is partly blocked.

DOI: 10.1103/PhysRevA.99.013817

I. INTRODUCTION

Abruptly autofocusing (AAF) beams have recently been intensively investigated theoretically [1] and experimentally [2,3], since the beams can abruptly concentrate the field intensity at a focal point while keeping almost constant intensity before the focal point, thus offering the possibility for laser ablation and biomedical treatment [1]. The AAF beams were first established based on radially symmetric Airy waves [1–3], also called circular Airy beams (CABs), and then were extended by introducing preengineered AAF beams with specific caustic trajectories [4], in which the angular spectrum representation method is applied to simply achieve the generation and control of AAF beams in Fourier space [2,5–7]. To better control the properties of AAF beams such as enhancement of the intensity contrast, locations of the focal point, specific caustic trajectories, and altering the focal pattern, diverse AAF beams have been proposed such as blocked CABs [6], modified CABs [7], AAF beams with preengineered caustics [4,8], autodefocusing and bottle beams [3,5,8], controllable AAF beams with linear optical potentials [9,10], high-power AAF beams with periodic lattices [11], and AAF vortex beams [12–15].

Very recently, nonparaxial AAF beams [16,17] with linear polarization and preengineered trajectories were proposed to generate a larger intensity contrast and smaller focus distance and spot size, resulting from the caustic engineering [16] or cooperative action of paraxial and nonparaxial energy flow [17]. The cylindrical vector AAF beams were also generated [18,19] and abrupt polarization transitions due to spin-orbit interaction were discussed for the vector AAF beams with spiral phase [18]. Nowadays, the AAF beams are widely used in the generation of a light bullet [20], advanced multiscale photopolymerization [21], AAF matter waves [22], and optical manipulations [3,23,24]. In particular for optical manipulations, it has been demonstrated in an experiment that Mie particles which are suspended in water solution and confined between two glass plates can be transversely trapped and manipulated via CABs [3]. Meanwhile, for Rayleigh particles immersed in linearly polarized CABs or modified CABs, theoretical analysis of radiation forces along the beam axis has been proposed [23,24] where the optical forces are evaluated within the dipole approximation. However, Mie particles appear in most optical manipulations, thus it is desirable to consider the optical interaction between CABs and Mie particles. Here we study the scattering problem of the CABs disturbed by a Mie particle with large size.

In this paper, based on the generalized Lorentz-Mie theory (GLMT) [25–27], the scattering problem of a spherical particle of an arbitrary size is solved exactly when it is

*huajinchen13@fudan.edu.cn
†syliu@zjnu.cn

immersed in the CABs of different polarizations, including linear, circular, radial, and azimuthal polarizations. Based on our exact solution, the AAF property and optical manipulation of CABs are explored and demonstrated. Starting with the angular spectrum representation, we work out the partial-wave expansion coefficients of the CABs for various polarizations. Then the theoretical formulas of the field distribution are derived to demonstrate the AAF property of the CABs. It is found that both the linear and circular polarizations are the best candidates to achieve the AAF, and the AAF property of the CABs is robust against blockage in the light path by a large particle before the focal point. Next we calculate the optical force acting on a particle located in the optical field of the CABs based on the Maxwell stress tensor method. The results show that, transversely, the Mie particle can be trapped only within the primary ring, while the side rings are not capable of confining the particle. Simultaneously, the transversely trapped Mie particle is accelerated along the curved trajectory towards the focal point and then it is pushed through the focal point, due to the absence of any longitudinal equilibrium near the focal point. In the region after the focal point of CABs, the morphed Bessel-like beam continues to confine the Mie particle transversely to the beam axis and simultaneously transports it along the straight beam axis over 100 wavelengths, due to its nearly nondiffractive property. In contrast, the CABs can stably trap a Rayleigh particle near the focal point in three dimensions, but it is hard to trap such a particle within the primary or side rings before the focal point, due to the perturbation by the Brownian force. The intriguing transport behavior of a Mie particle along a curved-and-straight trajectory, together with the robustness of AAF in turbulent environments, is expected to find application in the situation where a particle needs to be transported in a circumventing route.

II. RESULTS AND DISCUSSION

A. Exact solution of the scattering problem

In this section, starting with the angular spectrum representation and the GLMT, theoretical formulas are derived to exactly solve the scattering of a spherical particle with an arbitrary radius immersed in the CABs of different polarizations. Based on the angular spectrum representation method, the field profile of the incident CABs can be described by the angular spectrum of the field distribution on the initial plane with a field profile $E_0\mathrm{Ai}[(r_0-\sqrt{x^2+y^2})/w]\exp[\alpha_c(r_0-\sqrt{x^2+y^2})/w]$ [2], where r_0 is the radius of the primary ring, α_c is a decay parameter, and w and E_0 are the parameters to alter the width of the primary ring and the light beam power, respectively. If the center of the CABs is located at the point (x_b, y_b, z_b), then the incident CABs can be described via [28]

$$\mathbf{E}_i(x,y,z)=\iint_{-\infty}^{\infty}\mathbf{A}(\alpha,\beta)e^{i(k_x x+k_y y+k_z z)}d\alpha\,d\beta, \quad (1)$$

where (k_x, k_y, k_z) is the wave-number vector for each expanded plane wave with $k_x = k\sin\alpha\cos\beta$, $k_y = k\sin\alpha\sin\beta$, $k_z = k\cos\alpha$, and k the wave number in the background. The angular spectrum of the field distribution on the initial plane reads [5,7]

$$\mathbf{A}(\alpha,\beta)=\frac{E_0 w}{2\pi k_\perp}\sqrt{(k_\perp r_0+k_\perp^3 w^3)\left(k_\perp r_0+\frac{k_\perp^3 w^3}{3}\right)}\times e^{-\alpha_c k_\perp^2 w^2}e^{-i(k_x x_b+k_y y_b+k_z z_b)}\times J_0\left(k_\perp r_0+\frac{k_\perp^3 w^3}{3}\right)\mathbf{s}(\alpha,\beta), \quad (2)$$

where $k_\perp = k\sin\alpha$ is the transverse component of wave vector and $\mathbf{s}(\alpha,\beta)=(s_x, s_y, s_z)$ denotes the polarizations of each expanded plane wave with $s_z=-(s_x k_x/k_z + s_y k_y/k_z)$ based on the Maxwell equation $\nabla\cdot\mathbf{E}_i=0$. For instance, $(s_x, s_y)=(\cos\beta, \sin\beta)$ is for the radial polarization (also called TM mode) and $(s_x, s_y)=(-\sin\beta, \cos\beta)$ for the azimuthal polarization (also called TE mode).

Using the GLMT, the incident CABs can also be described in terms of the vector spherical wave functions (VSWFs) $\mathbf{N}_{nm}^{(1)}(k,\mathbf{r})$ and $\mathbf{M}_{nm}^{(1)}(k,\mathbf{r})$ [25–27,29],

$$\mathbf{E}_i(r,\theta,\phi)=-i\sum_{n,m}E_{mn}\left[p_{mn}\mathbf{N}_{nm}^{(1)}(k,\mathbf{r})+q_{mn}\mathbf{M}_{nm}^{(1)}(k,\mathbf{r})\right], \quad (3)$$

where the origin of spherical coordinates (r,θ,ϕ), corresponding to the Cartesian coordinates (x, y, z), is located at the sphere center and the factor $E_{mn}=E_0 i^n\gamma_{mn}$ with $\gamma_{mn}=[\frac{(2n+1)(n-m)!}{n(n+1)(n+m)!}]^{1/2}$. Based on the orthogonality of the VSWFs, the partial-wave expansion coefficients p_{mn} are derived via the integral

$$p_{mn}=C_p\int_0^{\pi}d\theta\int_0^{2\pi}d\phi(\mathbf{e}_r\cdot\mathbf{E}_i)P_n^m(\cos\theta)e^{-im\phi}\sin\theta,$$

where $\mathbf{e}_r$ is the unit vector in spherical coordinates, $P_n^m(\cos\theta)$ is the associated Legendre function of the first kind, and $C_p=\frac{i^{1-n}\gamma_{mn}kr}{4\pi E_0 j_n(kr)}$ is a coefficient factor with $j_n(kr)$ the spherical Bessel function of order n. After substituting the incident field of the CABs $\mathbf{E}_i(\mathbf{r},\theta,\phi)$, the partial-wave expansion coefficients p_{mn} read

$$p_{mn}=\frac{kw}{2}(-i)^m\gamma_{mn}^{1/2}e^{-im\psi_0}\int_{\alpha=0}^{\pi/2}e^{-ikz_b\cos\alpha}e^{-\alpha_c k_\perp^2 w^2}\times C(\alpha)Q(\alpha)J_0\left(k_\perp r_0+\frac{k_\perp^3 w^3}{3}\right)d\alpha,$$

with

$$C(\alpha)=\sqrt{(k_\perp r_0+k_\perp^3 w^3)\left(k_\perp r_0+\frac{k_\perp^3 w^3}{3}\right)}$$

and

$$Q(\alpha)=\begin{cases}[e^{i\psi_0}J_{m-1}(k_\perp\rho_0)-e^{-i\psi_0}J_{m+1}(k_\perp\rho_0)][s_x(i\tau_{mn}-\pi_{mn}\cos\alpha)+s_y(i\tau_{mn}+\pi_{mn}\cos\alpha)] & \text{(linear or circular)}\\ 2J_m(k_\perp\rho_0)\tau_{mn} & \text{(radial)}\\ -2J_m(k_\perp\rho_0)\pi_{mn}\cos\alpha & \text{(azimuthal)},\end{cases}$$

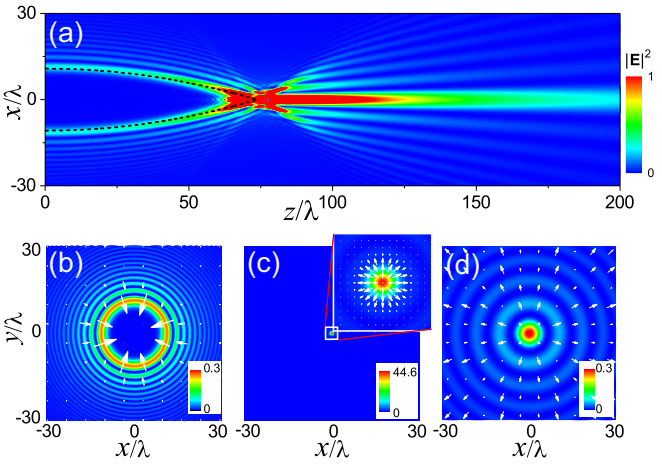

FIG. 1. Field intensity profiles of the incident CABs with linear polarization. (a) Longitudinal slice. Transverse slices are shown at different distance with (b) $z = 10\lambda$, (c) $z = f_{\mathrm{Ai}} \simeq 75\lambda$, and (d) $z = 180\lambda$. (c) Amplified view near the focal point with a square region from -2λ to 2λ. The white arrows denote the transverse Poynting vectors and the black dashed line in (a) is plotted via the analytic formula $R(z) \simeq r_0 + w - z^2/4k^2w^3$. The CABs have the parameters $(s_x, s_y) = (1, 0)$, $r_0 = 10\lambda$, $w = 1.5\lambda$, $\alpha_c = 0.05$, $E_0 = 1$, and $\lambda = 1.064\ \mu$m.

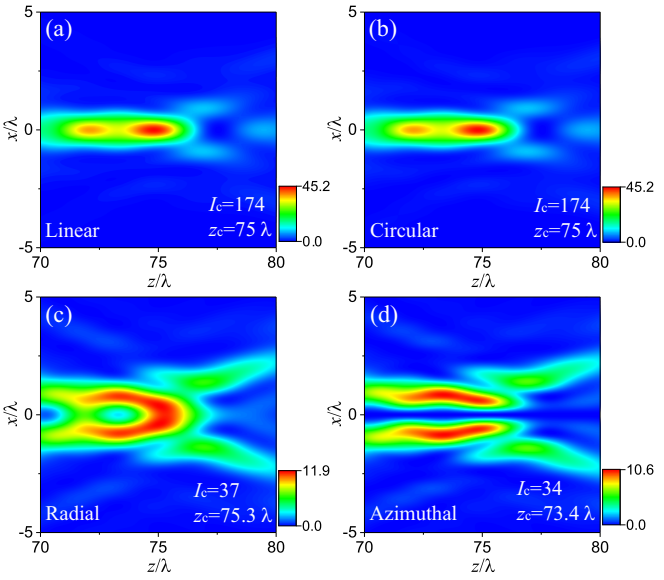

FIG. 2. Field distributions near the focal point on the slice with $y = 0$ for (a) linear ($s_x = 1, s_y = 0$), (b) circular ($s_x = 1, s_y = i$), (c) radial, and (d) azimuthal polarizations, where I_c and z_c denote the intensity contrast and position of the focal point, respectively.

where $(\rho_0 \cos\psi_0, \rho_0 \sin\psi_0)$ denotes the transverse location of the center of CABs corresponding to (x_b, y_b), with $x_b = \rho_0 \cos\psi_0$ and $y_b = \rho_0 \sin\psi_0$, and q_{mn} can be directly obtained by exchanging the factors τ_{mn} and π_{mn}. The factors $\pi_{mn} = m P_n^m(\cos\alpha)/\sin\alpha$ and $\tau_{mn} = d P_n^m(\cos\alpha)/d\alpha$ are two auxiliary functions. For the scattering field, it is obtained via [25–27,29]

$$\mathbf{E}_s(r, \theta, \phi) = i \sum_{n,m} E_{mn} \left[a_{mn} \mathbf{N}_{nm}^{(1)}(k, \mathbf{r}) + b_{mn} \mathbf{M}_{nm}^{(1)}(k, \mathbf{r}) \right], \tag{4}$$

where the Mie scattering coefficients a_{mn} and b_{mn} are given by $a_{mn} = a_n p_{mn}$ and $b_{mn} = b_n q_{mn}$, with a_n and b_n the Mie coefficients [30].

B. The AAF property of CABs

In this section, based on the above formulas, the field distribution of CABs is first simulated to show the AAF property, including the intensity contrast and focal distance of CABs. The AAF property of CABs for different polarizations is also demonstrated. In addition, it is shown that the AAF property of CABs is robust against the strong disturbance by a large-sized particle. Considering the linear polarization oscillating along the x axis (i.e., $s_x = 1$ and $s_y = 0$) as an example, the profile of incident field intensity in the x-z plane is demonstrated via Eq. (3) with the beam center $(x_b, y_b, z_b) = (0, 0, 0)$, as shown in Fig. 1(a). It is found that the field intensity of the CABs is abruptly concentrated at the focal point with focal distance $z_c = f_{\mathrm{Ai}} \simeq 75\lambda$ and the intensity contrast [1] reaches $I_c \simeq 174$, where the intensity contrast I_c is defined as a ratio of the field intensity at the focal point to that at the intensity extremum within the primary ring on the initial plane $z = z_b$ [1]. From Fig. 1(a) we can also find that the CABs nearly maintain a constant field intensity before the propagation distance $z = 50\lambda$ and tend to a Bessel-like beam after $z = 150\lambda$ [3,5,31]. Figure 1(b) suggests that the AAF property of CABs stems from the inward concentrated field intensity, where the transverse Poynting vectors denoted by the white arrows point towards the beam center. As the propagation distance increases, the mode area becomes small and reaches its minimum near the focal point at $z_c = f_{\mathrm{Ai}} \simeq 75\lambda$, as shown in Fig. 1(c), where the transverse Poynting vectors start changing the directions to point outward from the beam axis. With increasing the distance to $z = 180\lambda$, the magnitudes of transverse Poynting vectors are very small within the region of a central bright spot [see Fig. 1(d)], thus the morphed Bessel-like beam slightly diffracts after the focal point. Considering the curved trajectory of the intensity maximum for an Airy beam [32], the radius of the primary ring for the CABs reads $R(z) \simeq r_0 + w - z^2/4k^2w^3$, which is presented as a black dashed line in Fig. 1(a). The focal distance can also be obtained via $R(z) = 0$ and reads $z_c = 2kw^2\sqrt{r_0/w + 1} \simeq 78\lambda$ [17], which coincides well with the simulation result.

To demonstrate the AAF property of CABs influenced by different polarizations, profiles of field intensity near the focal point of the CABs with circular, radial, and azimuthal polarizations are plotted in Fig. 2. It can be seen that the linearly and circularly polarized CABs have almost the same profile of field intensity, and the distribution seems like a light bullet [20] in the region near the focal point [see Figs. 2(a) and 2(b)]. In contrast, for the radially and azimuthally polarized CABs in Figs. 2(c) and 2(d), the spot size near the focal point is larger and a hollow dark spot appears for the azimuthal polarization. One can also see from Fig. 2 that the intensity contrast reaches $I_c \simeq 174$ at the focal distance $z_c \simeq 75\lambda$ for the linear or circular polarizations, while it only reaches $I_c \simeq 37$ (34) at $z_c \simeq 75.3\lambda$ (73.4λ) for the radial (azimuthal) polarization. It

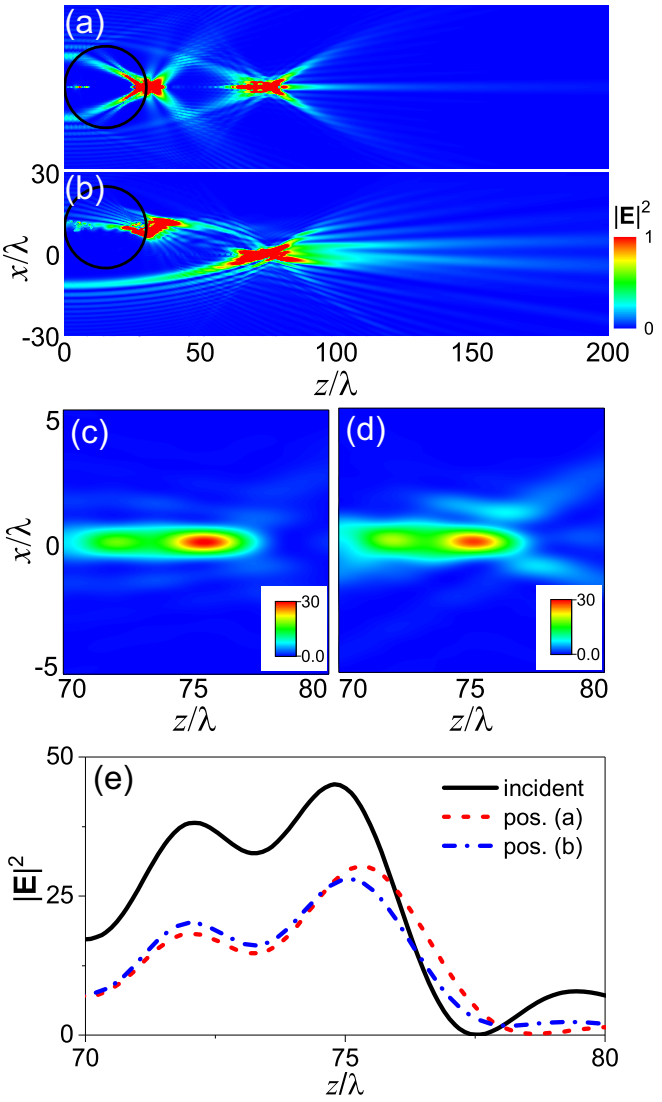

FIG. 3. Total field intensity profile of the AAF beam with linear polarization scattered by a dielectric sphere with radius $r_s = 15\lambda$ and permittivity $\varepsilon_r = 2.53$. The particle is located at the positions (a) $(0, 0, 15\lambda)$ and (b) $(10\lambda, 0, 15\lambda)$, where the black circles denote the dielectric particle. (c) and (d) Amplified views of field intensity corresponding to (a) and (b) near the focal point. (e) Field intensity along the z axis.

is concluded that the linearly or circularly polarized CAB is the best candidate to present the AAF property.

We next focus on the AAF property of the CABs strongly disturbed by a very large particle, where the dielectric particle has radius $r_s = 15\lambda$ and permittivity $\varepsilon_r = 2.53$, and the linear polarization is considered here as an example since it is one of the best candidates to present the AAF property. As shown in Fig. 3, profiles of total field intensity along the x-z plane are plotted for different particle positions, with the black circles denoting the dielectric particles. It can be seen that the field intensity is obviously disturbed by the large-sized dielectric particle [see Figs. 3(a) and 3(b)] and in particular the circular symmetry of CABs is broken for the particle position at $(10\lambda, 0, 15\lambda)$. Interestingly, the CABs can continue to be concentrated on the focal point after being scattered by the particle, although the field intensities near the focal point are slightly distorted, as can be seen from the amplified views in Figs. 3(c) and 3(d), corresponding to Figs. 3(a) and 3(b). A much clearer picture is presented in Fig. 3(e), where the total field intensity along the z axis is calculated for different particle positions. It can be found that the profiles of field intensity are similar to that without the particle disturbance, and the focal points are almost located at the same position $z_c = f_{\mathrm{Ai}} \simeq 75\lambda$, except that the amplitude of the field intensity has a small decay due to the strong scattering by the large-sized particle. Therefore, the AAF property of CABs is robust for the large-sized obstacle. In addition, we should note that the CABs have a radially symmetric Airy profile in the region before the focal point and asymptotically become Bessel-like beams [3,5,31] [see Fig. 1(a)]. For the Airy or Bessel beam, this has been used to show the self-healing effect [33,34] owing to their nondiffraction property. Similarly, the CABs can also self-heal the profiles of the field intensity after being disturbed by Mie particles.

C. Theoretical formulas of optical forces

Based on the exactly solved scattering problem of CABs and Mie particles, the optical manipulation of CABs by optical forces can also be described, in addition to the AAF property. The time-averaged optical force acting on a spherical particle is calculated by the integration of the Maxwell stress tensor over the outer surface S of the particle and reads [35,36]

$$F = \oint_S \mathbf{e}_r \cdot \langle \overleftrightarrow{\mathbf{T}} \rangle \, dS, \tag{5}$$

where $\mathbf{e}_r$ is the unit normal vector on the closed surface and the time-averaged Maxwell stress tensor reads $\langle \overleftrightarrow{\mathbf{T}} \rangle = \frac{1}{2}\mathrm{Re}[\varepsilon \mathbf{E}\mathbf{E}^* + \mu \mathbf{H}\mathbf{H}^* - \frac{1}{2}(\varepsilon \mathbf{E}\cdot\mathbf{E}^* + \mu \mathbf{H}\cdot\mathbf{H}^*)\overleftrightarrow{\mathbf{I}}]$, with $\overleftrightarrow{\mathbf{I}}$ being the unit tensor. Considering the lossless surrounding medium, the optical forces can be simplified to be express in terms of the partial-wave expansion coefficients [27,37–41]

$$\begin{aligned} F_1 &= \frac{2\pi\varepsilon}{k^2}|E_0|^2 \sum_{n,m} \left[c_{11}F_1^{(1)} - c_{12}F_1^{(2)} + c_{13}F_1^{(3)}\right], \\ F_2 &= -\frac{4\pi\varepsilon}{k^2}|E_0|^2 \sum_{n,m} \left[c_{21}F_2^{(1)} + c_{22}F_2^{(2)}\right], \end{aligned} \tag{6}$$

with the coefficients

$$\begin{aligned} c_{11} &= \left[\frac{(n-m)(n+m+1)}{n^2(n+1)^2}\right]^{1/2}, \\ c_{12} &= \left[\frac{n(n+2)(n+m+1)(n+m+2)}{(n+1)^2(2n+1)(2n+3)}\right]^{1/2}, \\ c_{13} &= \left[\frac{n(n+2)(n-m)(n-m+1)}{(n+1)^2(2n+1)(2n+3)}\right]^{1/2}, \\ c_{21} &= \left[\frac{n(n+2)(n-m+1)(n+m+1)}{(n+1)^2(2n+1)(2n+3)}\right]^{1/2}, \\ c_{22} &= \frac{m}{n(n+1)} \end{aligned}$$

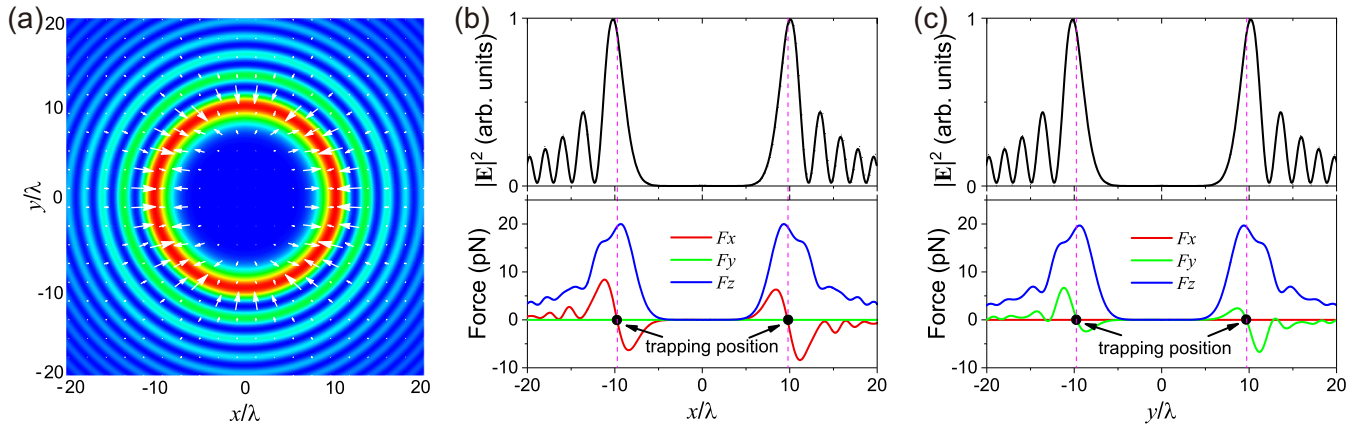

FIG. 4. (a) Transverse optical force distribution of a Mie particle. The white arrows denote the magnitude and direction of the transverse optical force in air; the incident intensity profile is also plotted as the background. Three components of optical force versus (b) the x axis and (c) the y axis in the plane $z = 25\lambda$. The particle has the radius $r_s = 2\lambda$ and permittivity $\varepsilon_r = 2.53$. The black circles denote the transverse trapping positions. The black solid lines denote the incident field intensity profiles in the plane $z = 25\lambda$ with arbitrary units.

and

$$
\begin{aligned}
F_1^{(1)} &= \tilde{a}_{mn}\tilde{b}^*_{m_1 n} + \tilde{b}_{mn}\tilde{a}^*_{m_1 n} - \tilde{p}_{mn}\tilde{q}^*_{m_1 n} - \tilde{q}_{mn}\tilde{p}^*_{m_1 n},\\
F_1^{(2)} &= \tilde{a}_{mn}\tilde{a}^*_{m_1 n_1} + \tilde{b}_{mn}\tilde{b}^*_{m_1 n_1} - \tilde{p}_{mn}\tilde{p}^*_{m_1 n_1} - \tilde{q}_{mn}\tilde{q}^*_{m_1 n_1},\\
F_1^{(3)} &= \tilde{a}_{mn_1}\tilde{a}^*_{m_1 n} + \tilde{b}_{mn_1}\tilde{b}^*_{m_1 n} - \tilde{p}_{mn_1}\tilde{p}^*_{m_1 n} - \tilde{q}_{mn_1}\tilde{q}^*_{m_1 n},\\
F_2^{(1)} &= \tilde{a}_{mn}\tilde{a}^*_{mn_1} + \tilde{b}_{mn}\tilde{b}^*_{mn_1} - \tilde{p}_{mn}\tilde{p}^*_{mn_1} - \tilde{q}_{mn}\tilde{q}^*_{mn_1},\\
F_2^{(2)} &= \tilde{a}_{mn}\tilde{b}^*_{mn} - \tilde{p}_{mn}\tilde{q}^*_{mn},
\end{aligned}
$$

where the indices $m_1 = m + 1$ and $n_1 = n + 1$ with the asterisk superscript denoting the complex conjugate and

$$
\begin{aligned}
\tilde{a}_{mn} &= a_{mn} - \tfrac{1}{2}p_{mn}, \quad \tilde{p}_{mn} = \tfrac{1}{2}p_{mn},\\
\tilde{b}_{mn} &= b_{mn} - \tfrac{1}{2}q_{mn}, \quad \tilde{q}_{mn} = \tfrac{1}{2}q_{mn}.
\end{aligned}
\tag{7}
$$

In Cartesian coordinates, three components of the optical force read

$$
F_x = \mathrm{Re}[F_1], \quad F_y = \mathrm{Im}[F_1], \quad F_z = \mathrm{Re}[F_2]. \tag{8}
$$

In the following numerical calculations of optical forces, the parameter is set to $E_0 = 1.7 \times 10^6$ V/m, corresponding to the field intensity of $I^0_{\max} = 1\ \mathrm{mW}/\mu\mathrm{m}^2$ at an intensity extremum within the primary ring in the initial plane $z = 0$, and the incident power of light beam reaches about 640 mW.

D. Optical manipulation of CABs for a Mie particle

In this section optical manipulation of CABs is discussed for a Mie particle located on different regions including the regions before, near, and after the focal point. Considering a Mie particle of radius $r_s = 2\lambda$ and permittivity $\varepsilon_r = 2.53$ (polystyrene beads with mass density $\rho_p = 1050\ \mathrm{kg/m}^3$) [27,42] on the plane $z = 25\lambda$ in air, the transverse optical force (F_x, F_y) is plotted as a function of particle positions along the x-y plane, as shown in Fig. 4, where the transverse optical forces are described by white arrows in the background of the intensity profile and the trapping positions in the transverse direction are denoted by black circles. The gravity of the Mie particle is ignored in the optical trapping since it reaches about 0.4 pN, which is much smaller than the optical forces of CABs. It can be found that the white arrows point towards the intensity extrema within the primary ring of CABs [see Fig. 4(a)], and the transverse optical forces become much smaller within the side rings. Thus the transverse optical forces have equilibrium positions near the intensity extrema within the primary ring, providing the possibility to transversely trap the particle. We also find that the profile of transverse optical forces is not circularly symmetric [see Fig. 4(a)], because the z component of field intensity I_z has dipolar structure for the linear polarization [16]. To present an even clearer picture, we have calculated optical forces versus the x and y axes as shown in Figs. 4(b) and 4(c), respectively. It can be seen that there exist trapping positions only within the primary ring, instead of side rings, so the Mie particle can only be transversely trapped within the primary ring, which is also demonstrated in the experiment [3]. When the Mie particle is located at these transverse trapping positions [see Figs. 4(b) and 4(c)], the longitudinal optical force F_z almost reaches its maximum to accelerate the Mie particle along the curved trajectory of CABs. Thus we can conclude that the Mie particle can only be trapped within the primary ring and then accelerated along the curved trajectory towards the focal point.

It is interesting to discuss the optical forces near the focal point, because the abruptly strong field intensity may lead to a very large optical gradient force. The distribution of optical forces on the Mie particle in the x-z plane is displayed in Fig. 5(a), where the black arrows denote the optical forces (F_x, F_z) and the incident field intensity is also demonstrated as the background. According to the directions of optical forces (F_x, F_z), one can clearly see that the transverse optical force F_x pushes the particle towards the beam axis and simultaneously the longitudinal optical force F_z accelerates the particle along the z axis and then moves it through the focal point. Meanwhile, the optical force F_x along the x axis and F_z along the z axis are also plotted in Figs. 5(b) and 5(c), respectively. It can be found that there exists a trapping position in the transverse direction [see Fig. 5(b)] and the transverse optical force F_x reaches its maximum of about 300 pN, which is large enough to achieve a stable transverse trapping.

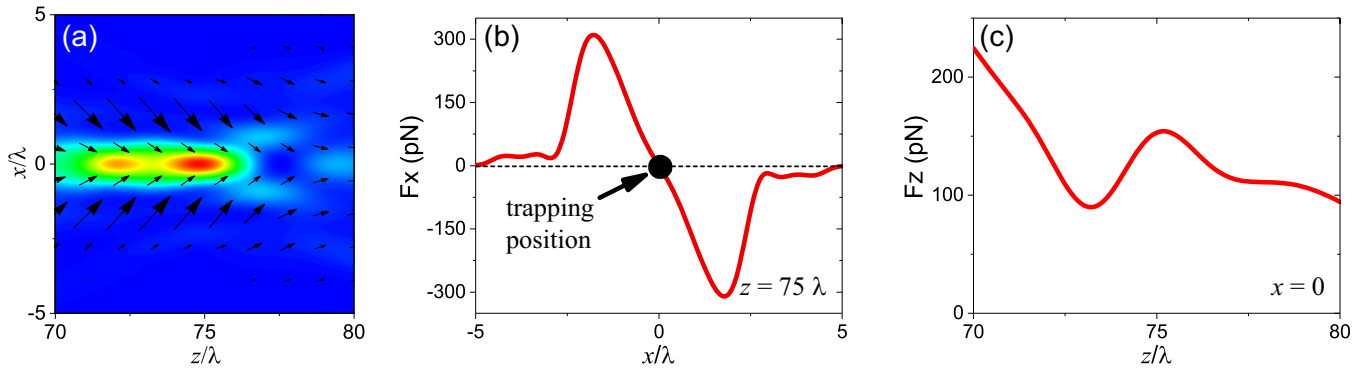

FIG. 5. (a) Distributions of optical forces (F_x, F_z) on the Mie particle near the focal point in the x-z plane, where the incident field intensity is also plotted as the background. Plot of (b) F_x along the x axis at $z = 75\lambda$ and (c) F_z along the z axis at $x = 0$. The black circle denotes the trapping position. All other parameters are the same as in Fig. 4.

However, the transversely trapped particle cannot be trapped in the longitudinal direction [see Fig. 5(c)] without a trapping position along the z axis, although the field intensity is very strong near the focal point, because the longitudinal scattering force prevails over the longitudinal gradient force near the focal point where the mode area is much smaller than the particle size. Thus the Mie particle can be transversely trapped near the focal point and simultaneously pushed through the focal point rather than be trapped therein.

As the Mie particle enters the region after the focal point, it can still be transversely trapped and transported along the beam axis. This is because the CAB in this region asymptotically becomes a Bessel-like beam, but with slight diffraction [see Fig. 1(a)]. The transverse trapping of the Mie particle is demonstrated in Fig. 6(a), where the transverse force F_x is plotted versus the x axis for different planes with $z = 100\lambda$, 200λ, and 300λ. It can be found that there always exists a transverse trapping position on the beam axis in different planes, and the magnitude of F_x reaches its maximum of 37.8, 4.2, and 1.2 pN corresponding to the plane with $z = 100\lambda$, 200λ, and 300λ, respectively. So the Mie particle will be transversely trapped near the beam axis after it is moved through the focal point by the optical forces. Meanwhile, the transversely trapped particle can be accelerated by the longitudinal force F_z along the beam axis over 100 wavelengths, as shown in Fig. 6(b), where the longitudinal force F_z reaches about 10 pN even in the plane $z = 300\lambda$. From Fig. 6(a) we also find that stiffness of the transverse trapping is reduced as the propagation distance of CABs increases. As a consequence, transversely, the Mie particle can be tightly trapped on the beam axis in the plane $z = 100\lambda$, while it is loosely trapped near the beam axis in the plane $z = 300\lambda$; this is also verified in the experiment [3]. The exotic curved-straight trajectory transport of Mie particles by the CABs may find applications in the case where the transport path is partly blocked.

E. Optical manipulation of CABs for a Rayleigh particle

In this section we discuss the optical manipulation of CABs for a Rayleigh particle immersed in the regions before and near the focal point. Although the radiation forces of a Rayleigh particle moving along the beam axis have been demonstrated within the dipole approximation [23], it is interesting to present the optical manipulation for a Rayleigh particle within the primary and side rings before the focal point. In this section we aim to find the critical condition of stable optical trapping for the Rayleigh particle within different regions, which can serve as a guide for both theorists and experimentalists.

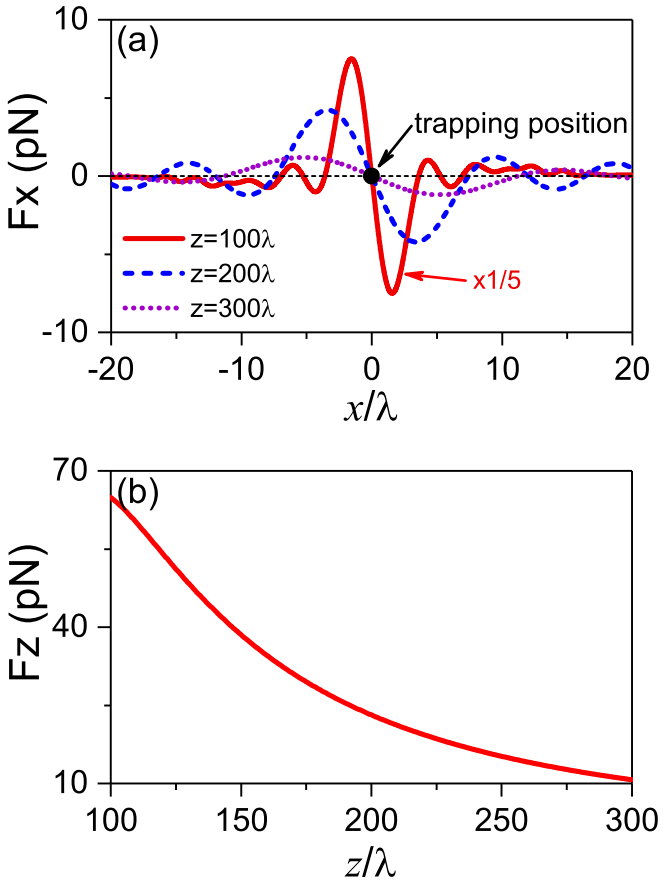

FIG. 6. Optical forces versus the particle positions. (a) Transverse optical force F_x versus the x axis in different planes with $z = 100\lambda$, 200λ, and 300λ, where the magnitude of the optical force for the plane $z = 100\lambda$ is scaled down to one-fifth. (b) Longitudinal force F_z versus the beam axis of CABs. The black circle denotes a trapping position. All other parameters are the same as in Fig. 4.

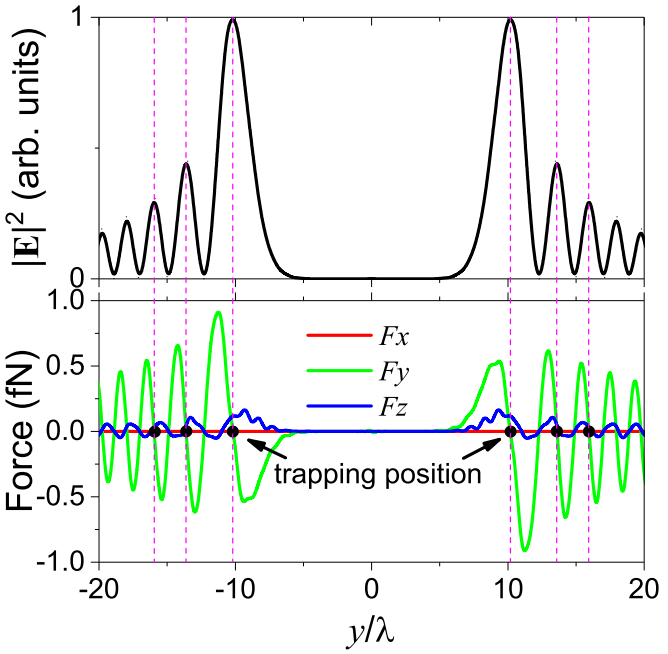

FIG. 7. Three components of optical force on a Raleigh particle of radius $r_s = 0.05\lambda$ and permittivity $\varepsilon_r = 2.53$ versus the y axis in the plane $z = 25\lambda$ in air. The trapping positions are denoted by the black circles and the incident field intensity profile in the plane $z = 25\lambda$ is also plotted with in arbitrary units.

Consider a Rayleigh particle of radius $r_s = 0.05\lambda$ and permittivity $\varepsilon_r = 2.53$ that is located in the region before the focal point on the plane $z = 25\lambda$, with the incident power of the light beam reaching about 640 mW. The gravity of the Rayleigh particle is ignored since it is only about 0.0065 fN. As shown in Fig. 7, three components of optical forces are plotted as a function of particle position along the y axis and the transverse trapping positions are denoted by black circles. It can be found that the transverse trapping positions of the Rayleigh particle are located at the intensity extrema within the primary and side rings of CABs, thus the Rayleigh particle might be transversely trapped within the primary or side rings by the optical gradient force. However, for the Rayleigh particle, the Brownian force due to the thermal motion might dominate and cannot be ignored. The maximum value of Brownian force reaches $F_b = \sqrt{12\pi\eta r_s k_B T} = 0.39$ fN [24,43,44] in air at room temperature $T = 300$ K, where the dynamic viscosity in air is $\eta = 1.85 \times 10^{-5}$ Pa s [45] and k_B is the Boltzmann constant. In order to achieve a stable trapping, the stability condition that optical forces must be much larger than the Brownian force F_b should be satisfied. It can be seen from Fig. 7 that the transverse optical force reaches its maximum of 0.89 fN and does not satisfy the stability condition. Thus the Rayleigh particle cannot be stably trapped in the transverse direction at these equilibrium positions due to the Brownian motion. It is also found that the longitudinal force F_z does not reach its extrema at these transverse trapping positions shown in Fig. 7, and F_z appears at negative values in some regions along the y axis, which is because the gradient force plays a leading role for the Rayleigh particle. Hence the Rayleigh particle cannot be accelerated along the propagation direction of CABs, for the incident power 640 mW of CABs. However, the optical forces can be enhanced when the incident power or the particle radius r_s increases, and thus the enhanced optical forces might overcome the Brownian force F_b to achieve a stable transverse trapping within the primary or side rings.

For the Rayleigh particle located near the focal point, we calculate the distribution of optical forces (F_x, F_z) as a function of particle position in the x-z plane, as shown in Fig. 8(a), where the black arrows denote the direction and magnitude of the optical force (F_x, F_z). In addition, we can see that the Rayleigh particle can be trapped near the focal point according to the directions of these black arrows. To demonstrate this point clearly, the optical force F_x along the x axis at $z = 75\lambda$ and F_z along the z axis at $x = 0$ are plotted in Figs. 8(b) and 8(c), respectively. One can see in Fig. 8(b) that a trapping position is located at the beam axis due to the strong gradient force. For the longitudinal force F_z along the z axis in Fig. 8(c), there exist two trapping positions, corresponding to the two intensity extrema near the focal point in Fig. 8(a). We also note that both the transverse optical force F_x and the longitudinal force F_z are much larger than the maximum absolute value of Brownian force $F_b \simeq 0.39$ fN. As a result, the Rayleigh particle can be stably trapped near the focal point in three dimensions by the strong optical gradient force due to the AAF property of CABs.

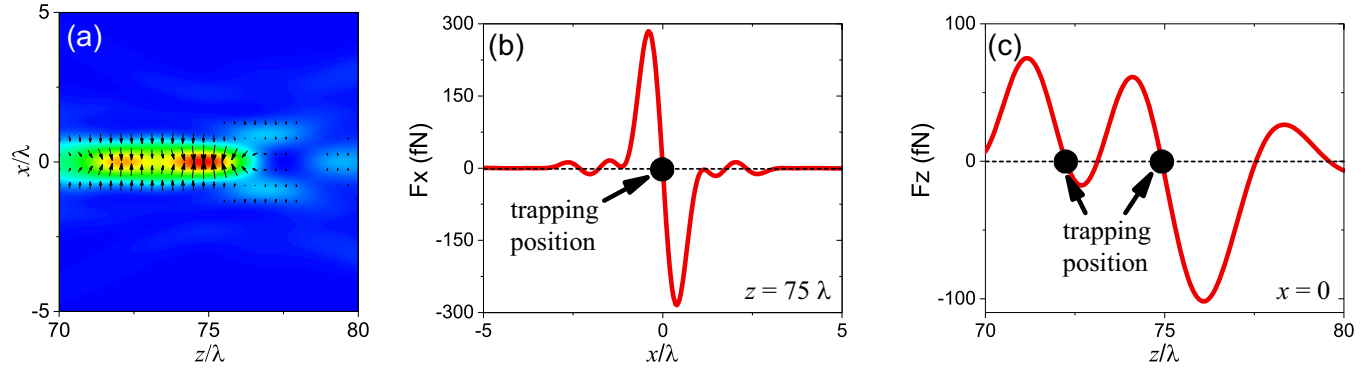

FIG. 8. (a) Distributions of optical forces (F_x, F_z) on the Rayleigh particle versus the particle positions near the focal point in the x-z plane, where the incident field intensity is also plotted as the background. Plot of (b) F_x along the x axis at $z = 75\lambda$ and (c) F_z along the z axis at $x = 0$. The black circles denote the trapping positions.

To establish a stable trapping of a small microparticle, the optical trapping potential energy should be large enough to overcome the kinetic energy of the particle in Brownian motion, satisfying the condition [43,46,47]

$$U(x, y, z) \geqslant 10 k_B T, \tag{9}$$

with the potential energy of the gradient force in air [47]

$$U(x, y, z) = \frac{2\pi r_s^3}{c}\left(\frac{\varepsilon_r - 1}{\varepsilon_r + 2}\right) I(x, y, z), \tag{10}$$

where c is the speed of light in vacuum and the potential energy is determined by the field intensity $I(x, y, z)$, the particle radius r_s, and the permittivity ε_r of the particle. By examining Eq. (10), it is found that the potential energy is proportional to the field intensity and the cube of the particle radius r_s while depending slightly on the permittivity ε_r. Considering the linear or circular polarization with the field intensity contrast $I_c = 174$, when the maximum of the field intensity on the initial plane is fixed to $I^0_{\max} = 1$ mW/μm ^{2} (corresponding to the incident power of 640 mW), there will exist a minimum of the particle radius about $r_s^{\min} = 180$ nm to achieve a stable trapping in the transverse direction within the primary ring before the focal point. In contrast, for a stable trapping near the focal point, the limit of particle size reaches only $r_s^{\min} = 32$ nm, based on Eqs. (9) and (10). Therefore, for an incident power of 640 mW, the particle with radius $r_s = 0.05\lambda$ discussed above is not transversely trapped within the primary ring before the focal point but can be stably trapped near the focal point. When the particle radius is set to $r_s = 0.05\lambda$, the parameter $I^0_{\max}$ must be larger than 39 mW/μm^2 (corresponding to an incident power of 25 W) to achieve a stable transverse trapping within the primary ring before the focal point, however, it is only $I^0_{\max} = 0.22$ mW/μm^2 (corresponding to an incident power of 141.5 mW) for a stable optical trapping near the focal point. Thus the Rayleigh particle with radius $r_s = 0.05\lambda$ is usually trapped near the focal point, but it is hard to be transversely trapped within the primary or side rings before the focal point of CABs, unless the CABs have a high enough incident power.

III. CONCLUSION

In summary, the scattering problem has been solved exactly when a spherical particle of an arbitrary radius is illuminated by the CABs with different polarizations, including linear, circular, radial, and azimuthal polarizations. Based on the accurate solution, the AAF property and optical manipulation of the CABs were discussed. The results demonstrate that both the linear and circular CABs are the best candidates to show the AAF property, which is also robust for the strong disturbance by a large-sized Mie particle. For the optical manipulation of a microparticle by optical forces, it was shown that a Mie particle with radius $r_s = 2\lambda$ and permittivity $\varepsilon_r = 2.53$ can be trapped transversely only within the primary ring and simultaneously accelerated along the curved trajectory of CABs. Then the trapped Mie particle will be pushed through the focal point, instead of being trapped near the focal point in three dimensions. Eventually, the particle will be transversely trapped near the beam axis and simultaneously transported along the beam axis over 100 wavelengths. In contrast, for a Rayleigh particle with radius $r_s = 0.05\lambda$, it can be stably trapped near the focal point in three dimensions via the strong optical gradient force due to the AAF property of CABs, when the incident power of the light beam reaches about 640 mW. However, it is hard to transversely trap the Rayleigh particle within the primary or side rings in the region before the focal point since the optical force acting on the particle cannot surpass the Brownian force from the thermal motion. Finally, the critical condition for stable optical trappings of the Rayleigh particle was discussed as well. The results might provide an additional degree of freedom for optical transport and trapping of microparticles.

ACKNOWLEDGMENTS

This work was supported by the National Natural Science Foundation of China (Grants No. 11404394, No. 11804061, No. 11747025, No. 11574055, and No. 11574275), Zhejiang Provincial Natural Science Foundation of China (Grant No. LR16A040001), Natural Science Foundation of Guangxi Province of China (Grant No. 2018JJB110016), Open Project of State Key Laboratory of Surface Physics in Fudan University (Grant No. KF2017_4), and Research Program of Science for Universities of Guang Xi Autonomous Region (Grant No. 2018KY0328).

[1] N. K. Efremidis and D. N. Christodoulides, Opt. Lett. **35**, 4045 (2010).
[2] D. G. Papazoglou, N. K. Efremidis, D. N. Christodoulides, and S. Tzortzakis, Opt. Lett. **36**, 1842 (2011).
[3] P. Zhang, J. Prakash, Z. Zhang, M. S. Mills, N. K. Efremidis, D. N. Christodoulides, and Z. Chen, Opt. Lett. **36**, 2883 (2011).
[4] I. Chremmos, N. K. Efremidis, and D. N. Christodoulides, Opt. Lett. **36**, 1890 (2011).
[5] I. Chremmos, P. Zhang, J. Prakash, N. K. Efremidis, D. N. Christodoulides, and Z. Chen, Opt. Lett. **36**, 3675 (2011).
[6] N. Li, Y. Jiang, K. Huang, and X. Lu, Opt. Express **22**, 22847 (2014).
[7] Y. Jiang, X. Zhu, W. Yu, H. Shao, W. Zheng, and X. Lu, Opt. Express **23**, 29834 (2015).
[8] I. D. Chremmos, Z. Chen, D. N. Christodoulides, and N. K. Efremidis, Phys. Rev. A **85**, 023828 (2012).
[9] C. Y. Hwang, K. Y. Kim, and B. Lee, IEEE Photon. J. **4**, 174 (2012).
[10] H. Zhong, Y. Zhang, M. R. Belić, C. Li, F. Wen, Z. Zhang, and Y. Zhang, Opt. Express **24**, 7495 (2016).
[11] P. Panagiotopoulos, D. G. Papazoglou, A. Couairon, and S. Tzortzakis, Opt. Lett. **39**, 4958 (2014).

[12] J. A. Davis, D. M. Cottrell, and D. Sand, Opt. Express **20**, 13302 (2012).
[13] Y. Jiang, K. Huang, and X. Lu, Opt. Express **20**, 18579 (2012).
[14] J. A. Davis, D. M. Cottrell, and J. M. Zinn, Appl. Opt. **52**, 1888 (2013).
[15] P. Li, S. Liu, T. Peng, G. Xie, X. Gan, and J. Zhao, Opt. Express **22**, 7598 (2014).
[16] R. S. Penciu, K. G. Makris, and N. K. Efremidis, Opt. Lett. **41**, 1042 (2016).
[17] M. Manousidaki, V. Y. Fedorov, D. G. Papazoglou, M. Farsari, and S. Tzortzakis, Opt. Lett. **43**, 1063 (2018).
[18] S. Liu, M. Wang, P. Li, P. Zhang, and J. Zhao, Opt. Lett. **38**, 2416 (2013).
[19] F. Wang, C. Zhao, Y. Dong, Y. Dong, and Y. Cai, Appl. Phys. B **117**, 905 (2014).
[20] P. Panagiotopoulos, D. Papazoglou, A. Couairon, and S. Tzortzakis, Nat. Commun. **4**, 2622 (2013).
[21] M. Manousidaki, D. G. Papazoglou, M. Farsari, and S. Tzortzakis, Optica **3**, 525 (2016).
[22] N. K. Efremidis, V. Paltoglou, and W. von Klitzing, Phys. Rev. A **87**, 043637 (2013).
[23] Y. Jiang, K. Huang, and X. Lu, Opt. Express **21**, 24413 (2013).
[24] Y. Jiang, Z. Cao, H. Shao, W. Zheng, B. Zeng, and X. Lu, Opt. Express **24**, 18072 (2016).
[25] G. Gouesbet and G. Gréhan, *Generalized Lorenz-Mie Theories* (Springer, Berlin, 2011).
[26] Y.-l. Xu, Appl. Opt. **34**, 4573 (1995).
[27] J. Ng, Z. F. Lin, C. T. Chan, and P. Sheng, Phys. Rev. B **72**, 085130 (2005).
[28] L. Novotny and B. Hecht, *Principles of Nano-optics* (Cambridge University Press, Cambridge, 2006).
[29] H. Chen, S. Liu, J. Zi, and Z. Lin, ACS Nano **9**, 1926 (2015).
[30] C. F. Bohren and D. R. Huffman, *Absorption and Scattering of Light by Small Particles* (Wiley, New York, 1983).
[31] C. Y. Hwang, K. Y. Kim, and B. Lee, Opt. Express **19**, 7356 (2011).
[32] W. Lu, H. Chen, S. Liu, and Z. Lin, Opt. Express **25**, 23238 (2017).
[33] G. A. Siviloglou, J. Broky, A. Dogariu, and D. N. Christodoulides, Phys. Rev. Lett. **99**, 213901 (2007).
[34] J. Broky, G. A. Siviloglou, A. Dogariu, and D. N. Christodoulides, Opt. Express **16**, 12880 (2008).
[35] J. D. Jackson, *Classical Electrodynamics*, 3rd ed. (Wiley, New York, 1999).
[36] Q. Ye and H. Lin, Eur. J. Phys. **38**, 045202 (2017).
[37] M. Liu, N. Ji, Z. Lin, and S. T. Chui, Phys. Rev. E **72**, 056610 (2005).
[38] Ø. Farsund and B. Felderhof, Physica A **227**, 108 (1996).
[39] J. P. Barton, D. R. Alexander, and S. A. Schaub, J. Appl. Phys. **66**, 4594 (1989).
[40] K. Dholakia and P. Zemánek, Rev. Mod. Phys. **82**, 1767 (2010).
[41] A. Salandrino, S. Fardad, and D. N. Christodoulides, J. Opt. Soc. Am. B **29**, 855 (2012).
[42] J. Chen, J. Ng, Z. Lin, and C. T. Chan, Nat. Photon. **5**, 531 (2011).
[43] H. Cheng, W. Zang, W. Zhou, and J. Tian, Opt. Express **18**, 20384 (2010).
[44] Z. Zhao, W. Zang, and J. Tian, J. Opt. **18**, 025607 (2016).
[45] W. M. Haynes, *CRC Handbook of Chemistry and Physics*, 96th ed. (CRC, Boca Raton, 2015).
[46] A. Ashkin, J. M. Dziedzic, J. E. Bjorkholm, and S. Chu, Opt. Lett. **11**, 288 (1986).
[47] Y. Harada and T. Asakura, Opt. Commun. **124**, 529 (1996).